sustainability

MDPI

Article

Multi-Model Rice Canopy Chlorophyll Content Inversion Based on UAV Hyperspectral Images

Hanhu Liu [1], Xiangqi Lei [1,*], Hui Liang [2] and Xiao Wang [3]

[1] College of Earth Sciences, Chengdu University of Technology, Chengdu 610059, China
[2] China Oil & Gas Pipeline Engineering Co., Langfang 065000, China
[3] College of Architecture and Civil Engineering, Chengdu University, Chengdu 610106, China
* Correspondence: 2022010036@stu.cdut.edu.cn

Abstract: Rice is China's main crop and its output accounts for 30% of the world's total annual rice production. Rice growth status is closely related to chlorophyll content (called Soil and Plant Analyzer Development (SPAD) values). The determination of a SPAD value is of great significance to the health status of rice, agricultural irrigation and regulated fertilization. The traditional SPAD value measurement method is not only time-consuming, laborious and expensive but also causes irreparable damage to vegetation. The main aim of the present study is to obtain a SPAD value through the inversion of hyperspectral remote sensing images. In order to achieve this purpose, the hyperspectral image of rice at different growth stages at the canopy scale was first acquired using a hyperspectral imaging instrument equipped with a drone; the spectral characteristics of the rice canopy at different growth stages were analyzed and combined with a ground-level measured SPAD value, the bands with high correlation between the SPAD values and the spectra of the rice canopy at different fertility stages were selected. Subsequently, we combined the spectral characteristics with the continuous projection algorithm to extract the characteristic band and used the PLS method in MATLAB software to analyze and calculate the weight of each type of spectral value and the corresponding canopy SPAD value; we then used the wavelength corresponding to the spectral value with the highest weight as the used band. Secondly, the four methods of univariate regression, partial least squares (PLS) regression, support vector machine (SVM) regression and back propagation (BP) neural network regression are integrated to establish the estimation model of the SPAD value of rice canopy. Finally, the models are used to map the SPAD values of the rice canopy. Research shows that the model with the highest decision coefficient among the four booting stage models is "booting stage-SVR" (R^2 = 0.6258), and the model with the highest decision coefficient among the four dairy maturity models is "milk-ripe stage-BP" (R^2 = 0.6716), all of which can meet the requirement of accurately retrieving the SPAD value of rice canopy. The above results can provide a technical reference for the accurate, rapid and non-destructive monitoring of chlorophyll content in rice leaves and provide a core band selection basis for large-scale hyperspectral remote sensing monitoring of rice.

Keywords: unmanned aerial vehicle (UAV); rice; hyperspectral images; chlorophyll; Soil and Plant Analyzer Development

check for updates

Citation: Liu, H.; Lei, X.; Liang, H.; Wang, X. Multi-Model Rice Canopy Chlorophyll Content Inversion Based on UAV Hyperspectral Images. *Sustainability* **2023**, *15*, 7038. https://doi.org/10.3390/su15097038

Academic Editors: Xiaoli Zhang, Dengsheng Lu, Xiujuan Chai, Guijun Yang and Langning Huo

Received: 3 March 2023
Revised: 8 April 2023
Accepted: 18 April 2023
Published: 22 April 2023

1. Introduction

Rice is China's main food crop [1–4]. Rice production is not only the basis for the economic development of agriculture, rural areas and farmers but also the cornerstone for promoting the healthy development of the national economy and ensuring national food security [5]. Chlorophyll, the main biochemical parameter in crops, is used to absorb light energy during the first stage of photosynthesis and plays a central role in light uptake in photosynthesis [6]. Its content can be used to reflect the photosynthetic capacity and nitrogen nutrient level of rice and to monitor the stress of heavy metal contamination in rice [7]. Therefore, the rapid and accurate acquisition of chlorophyll content in rice is of guiding significance for improving crop yield and quality.

Traditional methods for chlorophyll analysis mainly rely on field sampling, which is not only time-consuming but also inefficient [8]. This has somewhat limited our ability to monitor and manage crop growth and has prevented the development of precision agriculture efforts. With the vigorous development of remote sensing technology, a great deal has been achieved in the field of agriculture [9–11]. The advent of hyperspectral remote sensing has shifted the acquisition of crop information from traditional analytical methods to rapid, non-destructive, dynamic remote sensing monitoring [12]. At the same time, the development of small and light Unmanned aerial vehicles (UAVs) can effectively compensate for the high cost and complicated operation of traditional aerial photogrammetry [13,14]. Hyperspectral remote sensing has the monitoring function to monitor farm crop data, farm soil, crop quality, etc., continuously and dynamically grasp the growth of farm crops, to achieve quantitative, qualitative and positioning descriptions and analysis of farm crops so as to achieve the purpose of being an accurate operation. Huang Yayi [15] measured the chlorophyll content of Brassica napus with a UAV; Kim EJ et al. [16] compared spectral indices of two-dimensional river algae maps using a hybrid unmanned aerial vehicle (UAV) and unmanned surface vehicle (USV) system; Ballesteros et al. [17] used a UAV to measure maize and onion leaf area index in a semi-arid region of Spain; Calderón et al. [18] monitored early olive yellows disease based on a vegetation index using a UAV with a thermal imaging spectrometer. Canopy spectral information is a mixture of plant biochemical components, canopy structure, atmospheric and soil background, etc., and usually requires analysis of the spectral information according to the specific object of study [19,20]. Canopy spectral information is too complex, leading to complexities in sensitive band selection, parameter extraction, vegetation index construction, and predictive model construction for canopy spectral chlorophyll content monitoring [21–24]. It has been shown that the canopy spectrum is most sensitive to changes in chlorophyll content in the visible wavelengths [25,26]. Model simulations are used to find the bands that have the greatest influence of chlorophyll content and canopy reflectance. There are more studies on vegetation canopy spectra, and significant results have been achieved [27–29]; however, rice canopy spectra and chlorophyll content have not been studied much.

Therefore, this study uses a low-altitude UAV remote sensing platform equipped with a new imaging hyperspectral instrument (SENOP RIKOLA) to perform the inversion test on the SPAD value of the rice canopy. In order to achieve the purpose of regional monitoring of rice chlorophyll content, hyperspectral images are used. The main objectives are as follows: (1) Analyze the correlation between rice spectral information and SPAD values; (2) Extract sensitive bands at different reproductive stages; (3) Use four different types of rice canopy SPAD value inversion models to calculate SPAD values; (4) Conduct a comparative analysis to select the optimal inversion model for each reproductive period.

2. Materials and Methods

2.1. Overview of the Study Area

The field experiment area is located at Majouba, Jiangyou City, Sichuan Province, in the northeastern part of Sichuan Province, with the geographical coordinates of 105°05′08″ E, 32°05′35″ N. The region has favorable conditions for agricultural rice cultivation because of the synchronization of rain and heat, which can ensure the growth of rice and meet the heat requirements for the double ripening of rice in most parts of the territory. The red boxed area in Figure 1 shows the extent of the rice test field in the study area.

2.2. Composition of Remote Sensing System

The remote sensing system consists of a hyperspectral instrument and an unmanned aerial platform. The platform is a six-axis DJI M600 Pro UAV, which adopts the D-RTK GNSS system for positioning, and the ground platform uses the GJI GS pro software to plan the UAV flight path and set flight parameters. The hyperspectral instrument carried by the

UAV is the SENOP RIKOLA hyperspectral imager produced in Finland. This spectroscopic system can provide spectral images in the range from blue to near-infrared, with a spectral range of 490–900 nm. The resolution is 6.5 cm at a height of 100 m, the spectral resolution is up to 1 nm, and the number of effective wavelengths is 380.

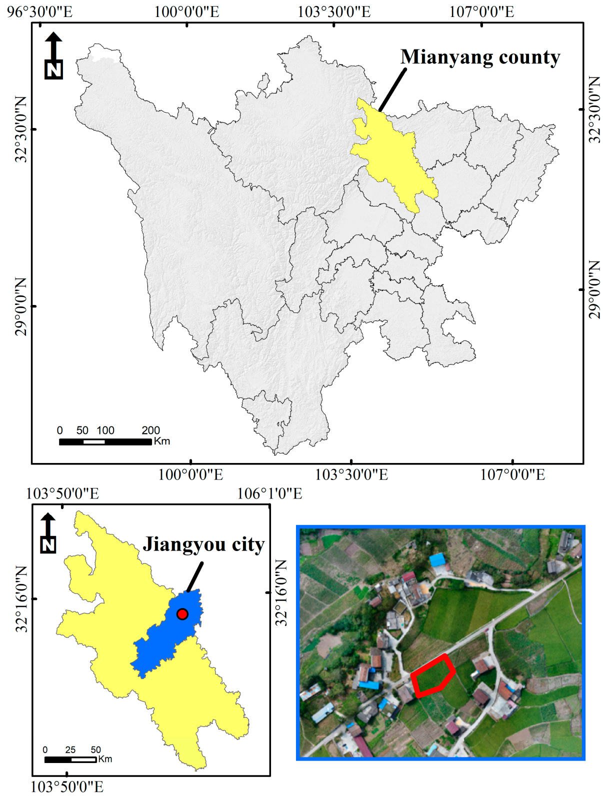

Figure 1. Location of the study area.

2.3. Image and Data Acquisition

2.3.1. Hyperspectral Image Acquisition

Hyperspectral images were first collected on 1 August 2019 from 11:00–13:00 in the test area with clear, windless and good visibility when rice was at the booting stage (the booting stage refers to the elongation and unfolding stage of the flag leaf of a cereal crop [30]), and then images were collected again at the milk-ripe stage (The milk-ripe stage is the early stage of seed filling of the rice spike, which is a critical period for rice yield improvement [31]). Before the flight mission started, the whiteboard was used to calibrate the hyper-spectrometer on the ground and correct the dark current. Set the flying height of the unmanned aerial vehicle to 120 m, set the speed to 5 m/s, and set the time interval for each hyperspectral image to 1.5 ms, the focal length to 9 mm, and the exposure time to 7 ms according to the intensity of sunlight. In this setting, the single frame coverage area of the image taken by the airplane is 14 m × 10 m.

2.3.2. Determination of SPAD Values of Rice Canopy in the Field

Spectral image acquisition was accompanied by the determination of rice canopy SPAD values in the experimental field. One hundred and twenty sample points were sampled evenly in the experimental field, five rice plants were randomly selected from each sample point, and two canopy leaves were selected from each rice plant; the total number of canopy leaves sampled was 1200. The SPAD values were then measured using a handheld chlorophyll meter, the SPAD-502 PLUS. Finally, the average measurement of the canopy of five rice plants was used as the SPAD value for this sample point. Figure 2 shows the UAV hyperspectral system and researchers sampling SPAD values in the field.

Figure 2. (**a**) Unmanned hyperspectral systems and (**b**) Sampling of SPAD value information in the field.

2.3.3. Hyperspectral Image Processing

When extracting the required information from the spectra of features, the large amount of "burr" noise in the spectral signal needs to be smoothed out in order to eliminate the effects of noise. In this paper, a median filter with a window of 3×3 was chosen to smooth the original spectrum of rice. Because of the intrinsic properties of rice reflectance spectra, this study performs a first-order derivative transformation of the raw hyperspectral information. After the original hyperspectral curve is de-enveloped, both absorption valleys and reflection peaks are highlighted, and the spectral curve is more clearly characterized. The method normalizes the curves to a consistent background, which facilitates comparison with other spectral curves and can then be used for spectral characterization and band selection [32].

2.3.4. Spectral Feature Analysis and Extraction of Sensitive Bands

Vegetation exhibits different spectral characteristics under different growth periods, fertilization conditions and environmental conditions and has different absorption and reflection effects on electromagnetic waves of different wavelengths. This characteristic of a substance's response to different wavelengths is its spectral signature. A correlation analysis was made between the SPAD value of rice canopy at different growth stages and the corresponding original hyperspectral spectrum and the first derivative spectrum and the de-envelope spectrum. The results are shown in Figure 3, and the correlation curves for the different fertility stages have similar patterns. The main manifestations are: (1) in the correlation curve between the SPAD values and the original hyper-spectrum (Figure 3a), the canopy SPAD values in the 550–728 nm range show a highly significant negative correlation with the spectral reflectance, and the extreme point wavelengths of the correlation coefficients are all around 623 nm. In the 679–763 nm range, the correlation changes from large to small and then large again. After 763 nm, the correlation coefficient tends to be stable, showing a significant positive correlation. (2) In the correlation curves between SPAD values and first-order derivative spectra (Figure 3b), the correlation curves fluctuate considerably from one fertility period to another, but the overall trend is similar in both fertility periods. The bands with high correlation are more prominent, and most of the bands with less correlation are filtered out, which shows that the first derivative spectrum can eliminate part of the background noise. (3) In the correlation curve between the SPAD value and the de-envelope spectrum (Figure 3c), the booting stage performs better in the green band, and the absolute value of the correlation R is 0.51. The milk-ripe stage is more stable than the booting stage. There is a trough near the red light band which is synchronized with the original spectrum. At this moment, the absolute value of the correlation coefficient is R = 0.49.

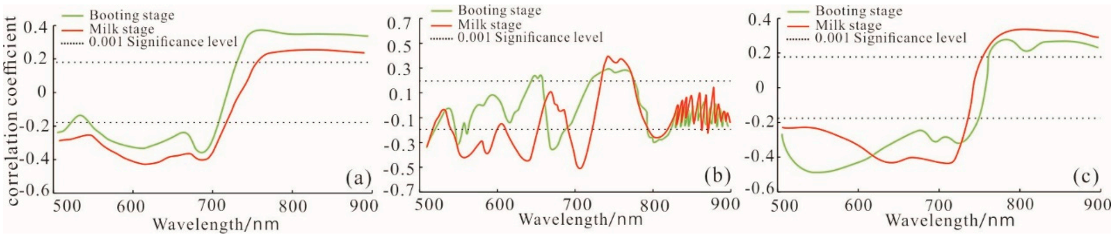

Figure 3. (**a**) Correlation of rice canopy SPAD values with original spectra, (**b**) first-order derivative spectra and (**c**) de-enveloped line spectra.

Based on the above analysis, the bands with a high correlation between the SPAD value of the rice canopy at different growth stages and the spectrum are selected, and then the continuous projection algorithm is used to extract the characteristic bands. In the MATLAB software, the PLS method is used to analyze and calculate the weight of each type of spectral value and the corresponding canopy SPAD value, and then the wavelength corresponding to the highest weighted spectral value is used as the sensitive band. The extraction results of the sensitive band are shown in Table 1.

Table 1. Selection of SPAD-sensitive bands in the rice canopy at different fertility stages.

Growth Periods	Spectral Types	Sensitive Bands (nm)
Booting stage	Original spectrum	567,686,770,818
	First derivative spectrum	539,560,728,755
	De-envelope spectrum	525,686,735
milk-ripe stage	Original spectrum	553,560,763
	First derivative spectrum	518,546,728
	De-envelope spectrum	647,728,818

2.4. Methods

2.4.1. Univariate Regression

The purpose of a regression analysis [33,34] is to explore the existence of a functional correlation between the independent variable (x) and the dependent variable (y), which can be expressed as a function $y = f(x)$. The essence of the regression equation $y = f(x)$ is the correlation between the measured and predicted values, and this correlation needs to be maximized by continuous fitting and adjusting functions between samples. The correlation between rice canopy SPAD values and hyperspectral characteristic parameters can be represented in several ways. We use several functions (Equations (1)–(4)) to fit the relationship between them to reach the optimal inversion.

$$y = a + bx \tag{1}$$

$$y = a + b\ln x \tag{2}$$

$$y = ae^{bx} \tag{3}$$

$$y = a + bx + cx^2 \tag{4}$$

where x is the spectral data characteristic parameter or sensitive band normalized value; y is the rice SPAD value; and a, b, and c are the regression coefficients.

2.4.2. Partial Least Squares Regression (PLSR)

PLSR is based on a combination of principal component analysis, multiple linear regression analysis and typical correlation analysis [35,36]. It was first used in the field of analytical chemistry but has since been widely used in various fields due to its better analytical capabilities. Compared with the commonly used principal component analysis or least square method, PLSR also considers the degree of explanation of the dependent variable (y) to the independent variable (x) and the respective principal components of y and x. When analyzing the principal components of the independent variable, if there is only one dependent variable, the effect of the dependent variable is accounted for, allowing the independent and dependent variables to participate in component extraction, thus retaining more valid information and making the regression results more stable. PLSR can generally reduce the collinearity between variables, extract the most useful information according to the principal component analysis method in the spectral information, and make the rice canopy SPAD value inversion model achieve higher accuracy.

In the PLSR, to determine whether the inverse ability of the model is improved by adding new principal components, a 5-fold cross-validation method is used to determine the inversion ability of the model corresponding to the number of different principal components, and therefore the cross validity Q_{h^2} should be determined (Equation (5)).

$$Q_{h^2} = 1 - \frac{press(h)}{ss(h-1)} \tag{5}$$

where press is the sum of squared prediction errors, h is the number of components, and ss is the sum of squared errors.

2.4.3. Support Vector Machine Regression (SVR)

The Support Vector Machine (SVM) is a binary model that defines the largest spacing on the feature space. The principle of SVM is to construct an optimal hyperplane (Figure 4) by projecting the input parameters into the high-dimensional space using nonlinear mapping and then solving the problem of nonlinear mapping by means of nuclear functions, thus making it easier to compute the high-dimensional data [37,38]. Support Vector Regression (SVR) also uses an optimal hyperplane to handle linear regression, but when dealing with nonlinear regression, it is solved by adding a kernel function, and the mathematical principle of SVR is shown below.

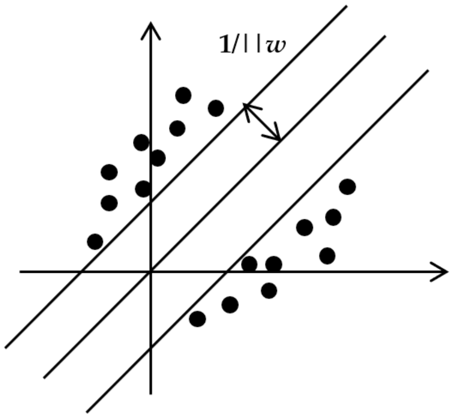

Figure 4. Optimal hyperplane.

Given a set of training samples X, x_i is the independent variable, yi is the dependent variable, and n is the number of samples. The idea of SVR is to find a function $f \in F$ to solve the problem of minimizing the nonlinear regression expectation risk R(f) by partitioning the hyperplane. F denotes the set of distributed functions, and the precision of the fitted sum is denoted by the error function coefficient ε. SVR solves the linear regression with a fitted function: $f(x) = wx + b$. x, w, and b represent the sample vector, normal vector, and offset of the regression function, respectively. This transforms the problem of solving the regression function into a convex quadratic linear planning problem according to the idea of categorically optimal hyperplanes. When it is difficult to partition the hyperplane in the linear case, sample points whose distance to the desired hyperplane is greater than 0 are introduced into the relaxation variable. The degree of penalty for sample points with deviations greater than ε depends on whether the constant C is greater than 0 and then introduces a Lagrangian function. The optimal programming problem is solved by solving its saddle point, transforming the original problem into a dual problem. From this, the optimal regression function (Equation (6)) can be obtained:

$$f(x) = \sum_{i=1}^{l} (\alpha_i^* - \alpha_i) \cdot (x_i \cdot x_k) + b \tag{6}$$

If the relationship between the input and output values of the modeled sample is nonlinear, then the sample points can be mapped to the high-dimensional feature space using the nonlinear function φ, allowing the nonlinear problem that is not easily solved in the low-dimensional space to be partitioned in the multidimensional space using the linear problem that is easily solved. In this way, only the function φ can be obtained, and the inner product operation in the high-dimensional space can be replaced by selecting the appropriate kernel function $K(x_i, x)$ so as to obtain the normal vector (Equation (7)) and the optimal regression function of the following regression function (Equation (8)):

$$w = \sum_{i=1}^{l} (\alpha_i - \alpha_i^*) x_i \tag{7}$$

$$f(x) = \sum_{i}^{l} (\alpha_i^* - \alpha_i) \cdot K(x_i, x) + b \tag{8}$$

SVR has a large number of advantages in solving the low number of modeling samples, especially in the difficult high-dimensional model nonlinearity problem and identification classification problem, by transforming the optimal hyperplane into a quadratic planning problem, thus achieving the advantages of easy training and applicability.

2.4.4. The BP Neural Network Regression

The artificial neural network is composed of a large number of nodes, which is a system that realizes intelligent processing or storage of information by simulating the human brain neural network. The BP neural network is the most widely used artificial neural network model due to its efficient multi-dimensional function mapping and excellent nonlinear processing capability [39,40]. Therefore, many scholars try to use the BP neural network to predict vegetation growth information and obtain good inversion results. The structure of the BP neural network is shown in Figure 5.

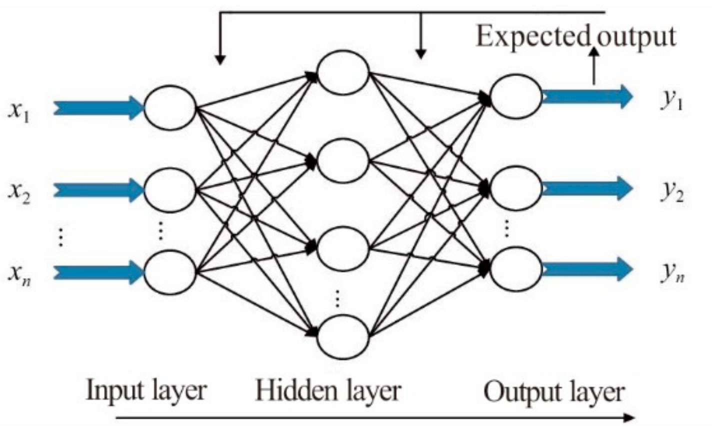

Figure 5. Schematic diagram of the BP neural network structure.

The process of signal processing by the BP neural network algorithm is divided into two main steps: the transmission of the received signal to the output layer and error feedback to the input layer. The above steps are embodied as follows: the input layer receives the input data, transmits the signal to the next layer through each node, and finally reaches the output layer after processing by the intermediate neural layer. The system compares the result of the output layer with the expected value and analyzes the error, then transmits the error back to the input layer in the incoming direction and adjusts the weights and thresholds of each neural layer in the process. The process is repeated, and the calculation is stopped when the output layer result is equal to the expected value.

The process by which the error is transmitted back to the input layer in the incoming direction is called reverse propagation of the error. It is the backward transmission of errors from the output layer to the input layer, where each neural layer adjusts the weights and thresholds of that layer based on the feedback values received. When the error of the BP neural network operation result is large, the "input-output-input" process is repeated. The specific steps of the system implementation are as follows: After receiving the signal at the input layer, let net_i be the signal value of the i-th node of the hidden layer in the system, and O_k the output value of the k-th node of the output layer. Assuming that there are P training samples, the error of the modeled sample data when the error is back-propagated is (Equation (9)):

$$E_p = \frac{1}{2}\sum_{p=1}^{p}\sum_{k=1}^{L}\left(T_k^p - O_k^p\right)^2 \tag{9}$$

The values of the connection parameters in the system are modified according to the gradient descent method in order to obtain the connection parameters for the output layer. Finally, by sequentially combining the output layer thresholds, implied layer weights and threshold changes, we can obtain the BP neural network input layer weights (Δw_{ij}), the input layer thresholds $\Delta\theta$_i, the corresponding output layer weights ($\Delta\theta_i$) and the threshold values (Δa_k).

The essence of the BP neural network algorithm is the selection of the most rapid descent method, which alternates between forward and backward work. Based on the error feedback received, the system modifies the weights and thresholds and repeatedly adjusts the parameters of each layer to the optimal effect so as to obtain the most suitable results.

3. Results and Discussion

3.1. Model Construction

3.1.1. Model Construction Based on Univariate Regression

In this study, the sensitive bands extracted from Table 1 are substituted into Table 2 (common vegetation monitoring parameters) according to the actual situation and in conjunction with previous studies so that each of these parameters has clear significance in this paper. Table 3 lists the parameters whose determination coefficient values (R^2) of canopy SPAD values and characteristic parameters are higher than 0.4 from 90 modeling samples selected from two growth periods. In Table 3, the characteristic parameters at the booting stage (DVI (R_{Nir}, R_{re}), RVI (S_{Dr}, S_{Db})) and milk-ripe stage (NDVI (R_{818}, R_{686}), DVI (R_{Nir}, Rre), CI (RNir, Rg), S_{Dr}) and the SPAD value of rice canopy R^2 reached more than 0.6, showing a very significant correlation.

From the correlation analysis in Table 3, it is known that these characteristic parameters cover several chlorophyll-sensitive bands such as green peak, red edge, red valley, and NIR in the range from 500 to 900 nm. Spectral parameters with R^2 above 0.6 are more in the milk-ripe stage than in the booting stage. We found that the rice plant just entered the growth and development stage at the booting stage; at this time, the single leaf area is small, and the chlorophyll content in the leaf is low. Therefore, this time the UAV hyperspectral instrument has a weak ability to capture canopy information. While the milk-ripe stage is the peak development period of rice plants, when the area of single leaf increases and the coverage is high, which is easy to be identified by the UAV hyperspectral instrument. Through the analysis and comparison of the results of eight groups of characteristic parameters, it is found that: in terms of weakening soil and environmental impact, the first-order micro classification parameters (S_{Dr}, RVI(S_{Dr}, S_{Db})) show a higher correlation than the soil regulation parameters (SAVI), indicating that the original spectrum can effectively weaken the impact of environmental noise after the first-order derivative transformation.

Table 2. Commonly used vegetation index and calculation formula.

Vegetation Index	Calculation Formulae or Definitions	Source of Formula
NDVI	$(R_{\lambda i} - R_{\lambda j})/(R_{\lambda i} + R_{\lambda j})$	[41]
DVI	$R_{Nir} - R_{re}$	[42]
SAVI	$1.5 \times (R_{\lambda i} - R_{\lambda j})/(R_{\lambda i} - R_{\lambda j} + 0.5)$	[43]
OSAVI	$(1 + 0.16)\ (R_{\lambda i} - R_{\lambda j})/(R_{\lambda i} + R_{\lambda j} + 0.16)$	[43]
TCARI	$3[(R_{\lambda i} - R_{\lambda j}) - 0.2(R_{\lambda i} - R_g)(R_{\lambda i}/R_{\lambda j})]$	[44]
MCARI	$[(R_{\lambda i}\text{-}R_{\lambda j}) - 0.2(R_{\lambda i} - R_g)](R_{\lambda i}/R_{\lambda j})$	[45]
RDVI	$\sqrt{NDVI \times DVI}$	[46]
MTCI	$(R_{\lambda j} - R_{\lambda i})/(R_{\lambda i} - R_{\lambda k})$	[47]
GRVI	$R_{\lambda i}/R_g$	[48]
RNDVI	$(R_{\lambda i} - R_{\lambda j})/\sqrt{R_{\lambda i} + R_{\lambda j}}$	[49]
CI	$R_{Nir}/R_g - 1$	[50]
RERDVI	$(R_{\lambda i} - R_{re})/\sqrt{R_{\lambda i} + R_{re}}$	[51]

Note: R_{Nir}, R_{re}, R_g, and R_λ represent the mean of the spectral band reflectance at NIR, red, green, and wavelength λ, respectively.

Table 3. Determination coefficient of SPAD value and characteristic parameters in rice canopy.

Characteristic Parameters	R^2	
	Booting Stage	Milk-Ripe Stage
NDVI (R_{818},R_{686})	0.5216	0.6015
DVI (R_{Nir},R_{re})	0.6252	0.6126
SAVI (R_{770},R_{647})	0.5317	0.5791
GRVI (R_{818},R_{518})	0.5864	0.5215
CI (R_{Nir},R_g)	0.5254	0.6136
S_{Dr}	0.5571	0.6042
RVI (S_{Dr},S_{Db})	0.6158	0.5181

3.1.2. Model Construction Based on Partial Least Squares Regression (PLSR)

Previous studies have shown that univariate regression yields good inversion accuracy. The use of PLSR regression was considered, and the multivariate input parameters based on principal component analysis were used as independent variables to invert the rice canopy SPAD values. The seven characteristic parameters (NDVI (R_{818}, R_{686}), DVI (R_{Nir}, R_{re}), SAVI (R_{770}, R_{647}), GRVI (R_{818}, R_{518}), CI (R_{Nir}, R_g), S_{Dr} and RVI (S_{Dr}, S_{Db})) in Table 3 and the sensitive bands in Table 1 were used as independent variables for the models of different parameter types to construct the PLSR-based inversion model of rice canopy SPAD values.

Characteristic parameter values for 90 modeling sample points at each fertility stage and the spectral band values of sensitive bands were applied to models with different parameter types. The correlation of different combinations is computed in MATLAB to implement the PLSR regression modeling to select the best inversion model for different types. Table 4 shows the construction and validation of the multivariate regression model for rice canopy SPAD values based on the PLSR algorithm.

Table 4. PLSR-based inversion model of SPAD values in rice canopy at different fertility stages.

Growth Stages	Parameters	Model Equations	R^2	RMSE
Booting stage	Feature parameters	$y = -0.551x_2 + 38.540x_3 - 0.103x_4 + 0.036x_6 + 2.846x_7 - 6.505$	0.6341	9.9688
	Original spectrum	$y = -0.515R_{567} + 1.445R_{686} + 0.585R_{770} + 1.017R_{818} - 44.006$	0.6115	19.528
	First derivative	$y = 3.713R_{539} - 0.578R_{560} + 1.082R_{728} - 0.577R_{755} + 7.575$	0.6150	16.0587
	De-envelope	$y = -0.455R_{525} + 1.650R_{686} + 1.709R_{735} - 24.809$	0.6176	7.5396
Milk-ripe stage	Feature parameters	$y = -32.968x_1 - 1.716x_2 - 4.567x_3 + 6.608x_4 + 0.925x_5 - 0.501$	0.6854	6.3586
	Original spectrum	$y = 1.536R_{553} - 0.190R_{560} + 0.625R_{763} + 0.941$	0.6181	22.5404
	First derivative	$y = 0.255R_{518} - 1.329R_{546} + 1.468R_{72}8 - 1.108$	0.6029	5.0406
	De-envelope	$y = -0.551x_2 + 38.540x_3 - 0.103x_4 + 0.036x_6 + 2.846x_7 - 6.505$	0.6011	26.8097

Note: x_1, x_2, x_3, x_4, x_5, x_6, x_7 are NDVI (R_{818}, R_{686}), DVI (R_{Nir}, R_{re}), SAVI (R_{770}, R_{647}), GRVI (R_{818}, R_{518}), CI (R_{Nir}, R_g), S_{Dr} and RVI (S_{Dr}, S_{Db}) at the corresponding values of each growth stage, R_λ represents the reflectance at the wavelength λ.

Comparing the model in Table 4 with the univariate model in the previous section shows that the overall inversion accuracy of the PLSR-based model is higher than the univariate regression of the model, and the R^2 models were all greater than 0.6. Among them, the highest value is based on the characteristic parameter model R^2 of the milk-ripe stage, which reaches 0.6854. At the same time, the overall accuracy of the characteristic parameter model is higher than that of the sensitive band model. It can be seen that the optimal model at the booting stage is "booting stage-PLSR", and its model equation is the corresponding characteristic parameter model at the booting stage in Table 4. The optimal model selection at the milk-ripe stage is consistent with the booting stage.

3.1.3. Model Construction Based on Support Vector Machine Regression (SVR)

In this study, seven characteristic parameters (NDVI (R_{818}, R_{686}), DVI (R_{Nir}, R_{re}), SAVI (R_{770}, R_{647}), GRVI (R_{818}, R_{518}), CI (R_{Nir}, R_g), SDr and RVI (SDr, S_{Db})) in Table 3 and the sensitive bands corresponding to each fertility stage in Table 1 were selected as input parameters to evaluate the prediction effect of different combinations using root mean squared error (RMSE). The input parameters of the final booting stage are "SAVI, GRVI and S_{Dr}", and the input parameters of the milk-ripe period are "DVI, SAVI, CI and S_{Dr}". Combined with previous experience, using Gaussian radial basis (RBF) as a nuclear function, the cross-validation method was used to generate in MATLAB software Optimal model to obtain the optimal parameters determined by the system (penalty factor C = 100, width factor = 0.1).

After determining the three parameters through experiments, the LIB SVM software package is called in MATLAB to establish the booting stage input parameters (SAVI, GRVI, S_{Dr}) and the milk-ripe stage input parameters (DVI, SAVI, CI, S_{Dr}). The parameters of the inversion model are shown in Table 5.

Table 5. SVR-based inversion model of SPAD values in rice canopy at different fertility stages.

Growth Stages	Input Parameters	Kernel Function	C	σ^2
Booting stage	SAVI, GRVI, S_{Dr}	RBF	100	0.1
Milk-ripe stage	DVI, SAVI, CI, S_{Dr}	RBF	100	0.1

Note: C and σ^2 are the penalty factor and width factor of the SVR model kernel function (RBF), respectively.

3.1.4. Model Construction Based on BP Neural Network Regression

For this test, the input layer, the implicit layer and the output layer are all one layer. According to the previous study, the inversion is better than the sensitive band when the characteristic parameters are used as input parameters. Five characteristic parameters at the booting stage (DVI, SAVI, GRVI, S_{Dr} and RVI) and five at the milk-ripe stage (NDVI, DVI, SAVI, CI and S_{Dr}) were selected according to the cumulative cross-validation value $Q_{h^2} > 0.5$. The following feature parameters are used as input layer data. The number of nodes in the implied layer is determined as five according to the formula $l = \sqrt{n+m} + a$, and the number of nodes in the output layer is one. Therefore, in this experiment, the BP neural network model for retrieving the SPAD value of the canopy at the booting stage and the milk-ripe stage of the experiment is that the input layer node is five, the hidden layer node is eight, the output layer node is one, and the training method is Trainlm training function, the training rate is 0.05.

We normalized the measured values of characteristic parameters and SPAD values from 90 modeled samples at each fertility stage using MATLAB. The software imports the modeling sample data and uses the Trainlm function to train the modeling sample data. At level 0.001, the network stops training. After several training sessions, the model tends to be stable, and the output results no longer change. Therefore, the internal parameter values of the BP neural network model finally constructed during the two growth periods are shown in Tables 6–9.

Table 6. Input-hidden layer parameters of BP neural network at booting stage.

Hidden Layer Weights / Input Layer Weights	1	2	3	4	5	6	7	8
1	0.2165	1.2019	1.2364	−1.1247	−1.1021	0.5656	0.3653	1.0321
2	−1.8763	0.3487	0.7825	−0.9571	−1.9274	1.1894	0.7453	0.7985
3	1.0912	−0.9875	−0.6873	0.2094	1.3595	−0.1209	−1.2673	1.8632
4	0.2317	0.5423	−0.4501	1.7389	1.6120	−0.1075	1.2984	−0.5417
5	−0.7612	1.3211	1.2938	−0.5210	−1.9127	−1.0836	−0.1279	−1.8237
Threshold (b)	2.1835	−1.5408	1.7225	0.7613	0.9187	−0.6521	1.2013	−1.6091

Table 7. Output-hidden layer parameters of BP neural network at booting stage.

Hidden Layer Nodes	Weights	Threshold	Hidden Layer Nodes	Weights	Threshold
1	1.9812	0.472	5	−0.3017	0.472
2	0.4709		6	1.0145	
3	−1.3747		7	0.6430	
4	−0.5862		8	−1.5436	

Table 8. Input-hidden layer parameters of BP neural network at milk-ripe stage.

Hidden Layer Weights / Input Layer Weights	1	2	3	4	5	6	7	8
1	1.1904	−0.8730	0.5134	−0.8107	1.3467	0.7564	1.3875	−1.3108
2	0.7237	1.5719	−1.7891	1.3416	0.9134	−1.1876	0.1283	1.0234
3	−1.5064	0.3781	−0.3475	−1.9871	−0.3453	−0.6034	−0.8967	0.3246
4	0.3984	−1.0137	−0.4501	0.3401	1.7486	1.8793	−1.4113	1.2803
5	−1.1350	1.4503	1.2938	−0.0519	−0.5348	−1.0434	0.1987	−1.3146
Threshold (b)	1.1701	−1.1746	−0.3114	0.3260	−0.7408	−1.8430	−0.7634	0.8753

Table 9. Output-hidden layer parameters of BP neural network at milk-ripe stage.

Hidden Layer Nodes	Weights	Threshold	Hidden Layer Nodes	Weights	Threshold
1	−1.4578	0.5015	5	1.3014	0.5015
2	−0.3418		6	0.4357	
3	2.0134		7	−1.5834	
4	1.3619		8	0.3101	

3.2. Model Accuracy Analysis

3.2.1. Univariate Model Accuracy Analysis

The characteristic parameters with R^2 above 0.6 in Table 3 were selected to construct an inversion model of the SPAD value of the rice canopy. The spectral values of 30 test sample points at each fertility stage in the experimental field were substituted into the above model as independent variables and canopy SPAD values as dependent variables. The prediction accuracy of the model was checked in SPSS software using three statistical indicators: coefficient of determination (R^2), root mean square error (RMSE) and mean relative error (RE). The closer the R^2 is to one, the smaller the RMSE and RE, indicating higher model accuracy, and the results of the analysis are shown in Figure 6 and Table 10.

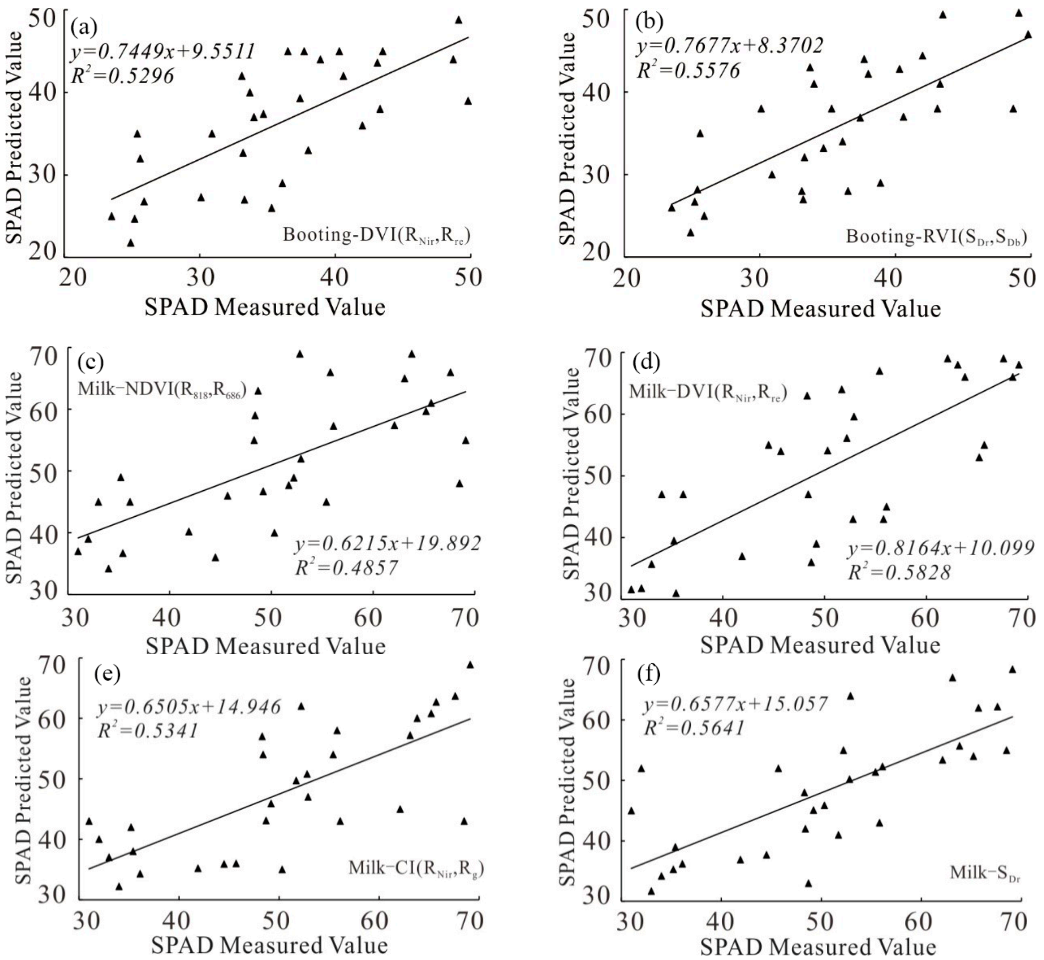

Figure 6. Correlation analysis between measured and predicted SPAD values in the rice canopy based on univariate regression (**a**) Booting stage-DVI(R_{Nir},R_{re}); (**b**) Booting stage-RVI(S_{Dr},S_{Db}); (**c**) Milk-ripe stage-NDVI(R_{818},R_{686}); (**d**) Milk-ripe stage-DVI(R_{Nir},R_{re}); (**e**): Milk-ripe stage-CI(R_{Nir},R_g); (**f**) Milk-ripe stage-S_{Dr}).

Table 10. Univariate regression-based inversion model accuracy check of rice canopy SPAD values.

Models		Model Equations	R^2	RMSE	RE
Booting stage	DVI(R_{Nir},R_{re})	$y = 74.486x^{0.8695}$	0.5296	5.29	14.6
	RVI(S_{Dr},S_{Db})	$y = -0.0629x^2 + 4.3705x + 9.9008$	0.5576	5.15	14.3
Milk-ripe stage	NDVI(R_{818},R_{686})	$y = 70.601x + 6.1291$	0.4857	7.73	15.3
	DVI(R_{Nir},R_{re})	$y = -10.817x^2 + 101.17x + 17.075$	0.5828	6.99	15.1
	CI(R_{Nir},R_g)	$y = 0.1896x^2 + 5.0079x + 25.901$	0.5341	7.35	16.3
	S_{Dr}	$y = 0.0055x^2 + 1.7285x - 13.78$	0.5641	8.53	14.5

Based on the test results, the coefficient of determination of the booting stage model "booting stage-RVI (S_{Dr}, S_{Db})" (R^2 = 0.5576) is closer to one. The root mean square error (RMSE = 5.29) and the relative error (RE = 14.6) are smaller, which indicates that the model "booting stage-RVI (S_{Dr}, S_{Db})" with greater predictive power and accuracy. In the same analysis, the corresponding model "milk-ripe stage-DVI (R_{Nir}, R_{re})" has a higher predictive power and accuracy during the milk-ripe stage and therefore can be used as an inverse model for the respective fertility period.

3.2.2. PLSR Model Accuracy Analysis

In the MATLAB software, the spectral values of the 30 test samples at each fertility stage of the test field were substituted into the optimal models in Table 4 ("booting stage-PLSR" and "milk-ripe stage-PLSR"). The predicted SPAD values for the sample points were obtained and then fitted and analyzed to the measured SPAD values, and the estimation capability and accuracy of the model were checked using R^2, RMSE, and RE, the results of which are shown in Figure 7 and Table 11.

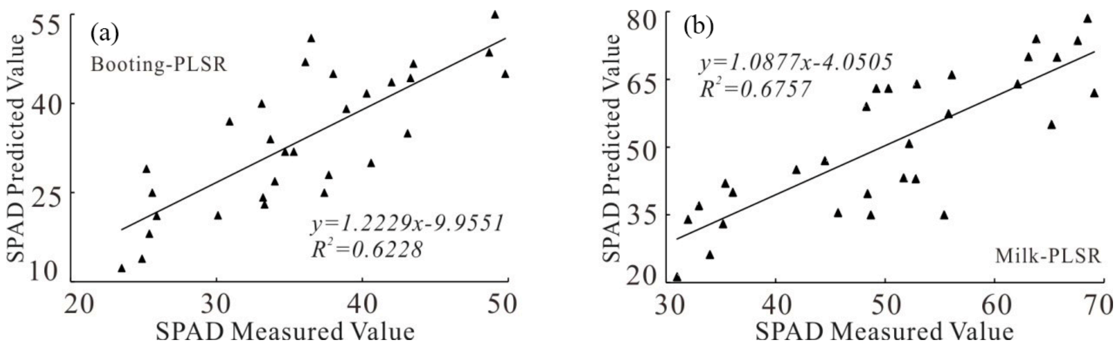

Figure 7. Correlation analysis between measured and predicted SPAD values in rice canopy based on the PLSR model (**a**) Booting stage-PLSR; (**b**) Milk-ripe stage-PLSR.

Table 11. PLSR-based accuracy check of rice canopy SPAD value inversion models.

Growth Stages	Models	R^2	RMSE	RE
Booting stage	Booting stage-PLSR	0.6228	7.17	21.2
Milk-ripe stage	Milk-ripe stage-PLSR	0.6757	9.12	17.9

Comparing the inversion results of the modeled samples with the test samples in the PLSR model shows that the R^2 and RMSE results of the modeled samples are similar to those of the test samples. This indicates that PLSR-based multiple regression models have good stability and generalizability. This shows that when inverting rice canopy SPAD values, the PLSR model is effective in inverting rice canopy SPAD values based on the structural robustness of the PLSR model; even if a certain input parameter changes, it is not easy to affect the overall inversion effect.

3.2.3. SVR Model Accuracy Analysis

According to the above study, under the optimal condition of each parameter, the inversion model of SPAD values in rice canopy based on the SVR algorithm was set as "booting stage-SVR" and "milk-ripe stage-SVR" at two reproductive stages. The spectral values of the 30 test sample points at each fertility stage were then substituted into the model to obtain the predicted SPAD values of the sample points, which were fitted to the measured SPAD values for analysis, and the predictive ability and accuracy of the model were tested using R^2, RMSE, and RE, with the results shown in Figure 8 and Table 12.

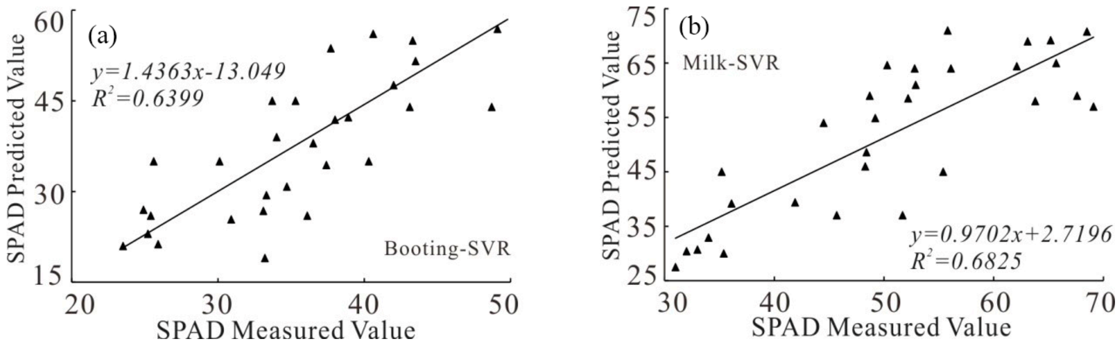

Figure 8. Correlation analysis between measured and predicted SPAD values in the rice canopy based on SVR models (**a**) Booting stage-SVR; (**b**) Milk-ripe stage-SVR.

Table 12. SVR-based accuracy check of rice canopy SPAD value inversion models.

Growth Stages	Models	R^2	RMSE	RE
Booting stage	Booting stage-SVR	0.6399	6.56	16.3
Milk-ripe stage	Milk-ripe stage-SVR	0.6825	8.11	14.7

From Figure 6, it can be seen that the SVR model is better predicted and the model accuracy has improved. The dispersion between the predicted and measured values of the SPAD values on the graph is low and overall realistic. Combined with Table 5, it is found that the RMSE and RE of both fertility groups are lower than those in the previous section, indicating that the SVR model can effectively predict rice canopy SPAD through machine learning to further improve the model prediction accuracy.

3.2.4. BP Neural Network Model Accuracy Analysis

The optimal inversion models of rice canopy SPAD values were set as "booting stage-BP" and "milk-ripe stage-BP" for each fertility stage, respectively. The remaining 30 test sample values from each fertility stage were then substituted into the model to obtain the SPAD values for different fertility stages in the rice canopy. The predicted and measured SPAD values were fitted and analyzed in MATLAB software to check the predictive ability and accuracy of the model using three parameters: R^2, RMSE, and RE, and the results are shown in Figure 9 and Table 13.

Table 13. Accuracy check of BP neural network-based inversion model for rice canopy SPAD values.

Growth Stages	Models	R^2	RMSE	RE
Booting stage	Booting stage-BP	0.6537	5.68	15.2
Milk-ripe stage	Milk-ripe stage-BP	0.7076	8.22	17.6

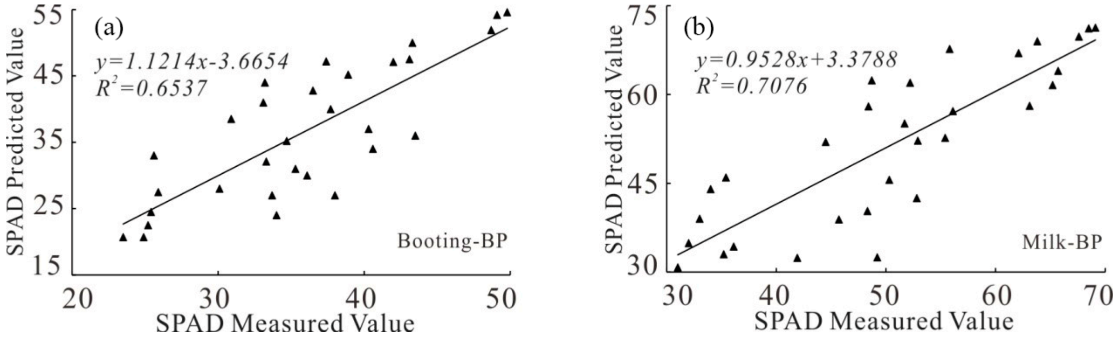

Figure 9. Correlation analysis between measured and predicted SPAD values in rice canopy based on BP neural network (**a**) Booting stage-BP; (**b**) Milk-ripe stage-BP.

From Figure 9 and Table 13, it can be seen that the BP neural network model performs better during the inversion of the coronal SPAD values in both fertility stages. In particular, in the analysis of the fit between predicted and measured values at the milk-ripe stage, R^2 reached above 0.7 for the first time, reflecting a very good inversion of the Effect. In addition, the RMSE value is smaller while obtaining a higher R^2, and the distribution of test sample point values is more uniform in the figure, which shows that the BP neural network can be effectively used in the rice canopy SPAD value inversion test.

3.3. Optimal Inversion Model Selection

The spectral data from the two reproductive periods in the study area were solved using the corresponding four optimal models to fill in the figure. Since there are only 120 sample points in total, it is difficult to be sure of the accuracy of the inversion if it is validated using a point-to-point approach. Therefore, nine sample points are used as a unit, that is, a similar smooth method is used to randomly sample the study area in a 4 m × 4 m window, and the inversion accuracy is evaluated based on the correlation between the measured mean and predicted mean of the sample points in each unit. Twenty research areas were collected for each growth period (Figure 10).

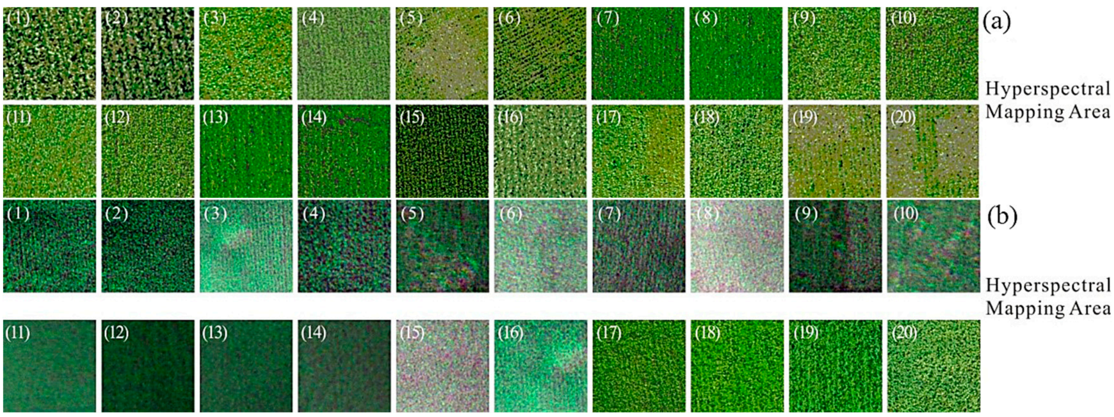

Figure 10. Mapping sample areas of booting and milk-ripe stage (**a**) Booting stage; (**b**) Milk-ripe stage.

The specific implementation steps are: (1) use the ENVI software to obtain the spectral reflectance values of the image pixels in the study area; (2) the spectral values are substituted for the feature parameters into the model to get the value of feature parameters, and the value of feature parameters as input parameters into the model to perform the operation to get SPAD prediction values; (3) dividing the SPAD prediction values into different levels, which are represented in the ENVI software with different color gradations, to obtain a SPAD value inversion chart (Figure 11).

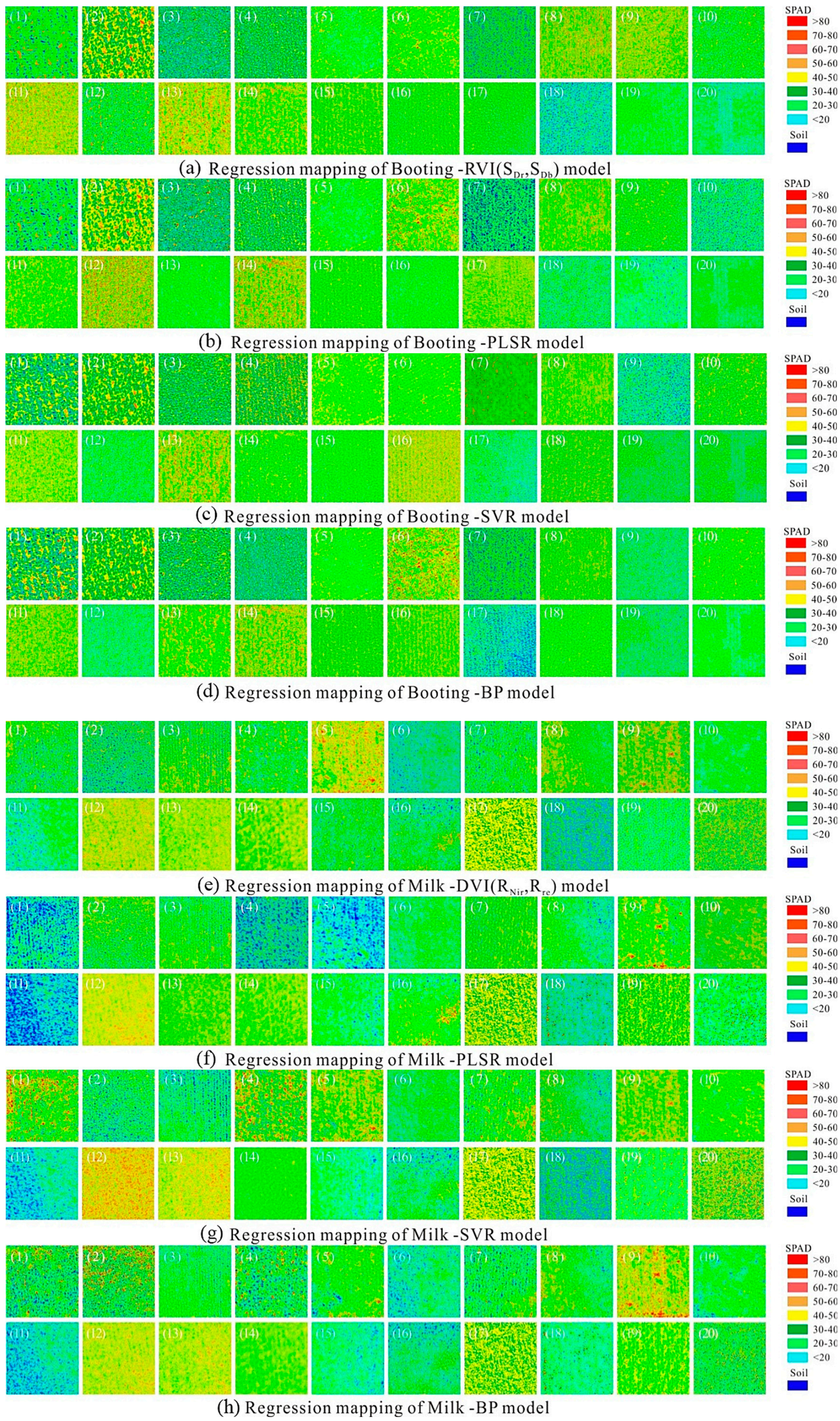

Figure 11. Distribution of SPAD value in rice canopy at different growth stages (**a**) Regression mapping of Booting-RVI(S_{Dr},S_{Db})model; (**b**) Regression mapping of Booting-PLSR model; (**c**) Regression mapping of Booting-SVR model; (**d**) Regression mapping of Booting-BP model; (**e**) Regression mapping of Milk-DVI(R_{Nir},R_{re}) model; (**f**) Regression mapping of Milk-PLSR model; (**g**) Regression mapping of Milk-SVR model; (**h**) Regression mapping of Milk-BP model.

It can be seen from the inversion results that the overall SPAD value at the booting stage is lower than that at the milk-ripe stage. The mean SPAD values in most field plots were in the 20–50 range during the booting stage, which is more consistent with the lower SPAD values in the rice canopy during the actual booting stage. The model "booting stage-SVR" has fewer outliers and no low or high values for the whole area, which is better. In contrast, during the milk-ripe stage, rice development is vigorous, and most of the rice canopy has high SPAD values, with many areas having SPAD values of 70 and above. Therefore, there are more orange-red color parts in the SPAD value inversion diagram, which contrasts with soil blue, and the gaps in the test field are distinct, but further model accuracy check is needed to select the most suitable inversion model for each fertility stage. In order to check the accuracy of the fill-in maps, the mean of the inversion plot SPAD values was fitted to the mean of the measured values at the sample points (Figures 12 and 13). In the case where the RMSE is minimum, the slope and R^2 are closest to one, and the closer the fitting result is to the 1:1 line (dashed line in the above figures), the more accurate the estimation result is. It can be seen that among the four test models at the booting stage, the regression slope (1.2626) and the determination coefficient (R^2 = 0.6258) of the "booting stage-SVR" model are closest to one, and the root mean square error is the smallest (RMSE = 7.3651). The inversion estimates the highest accuracy of the mapping results. In the four models of the milk-ripe stage test, the regression slope (1.0868) and the coefficient of determination (R^2 = 0.6717) of the "milk-ripe stage-BP" model are closest to one, and the root mean square error is the smallest (RMSE = 6.3266). The inversion estimates the highest accuracy of the mapping results.

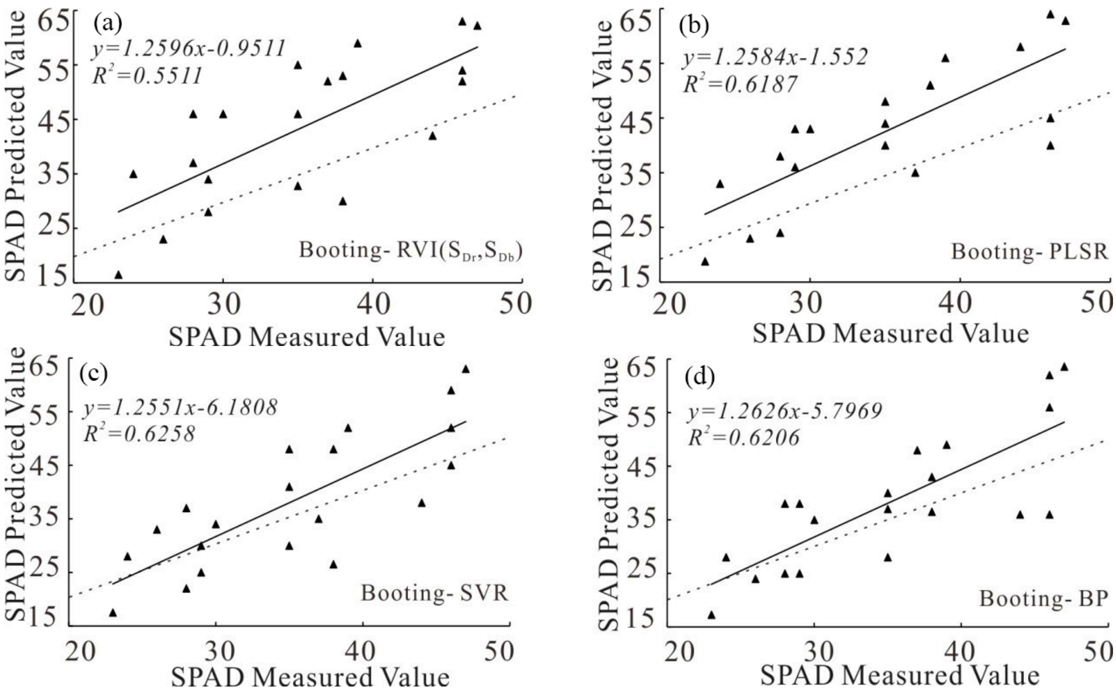

Figure 12. Mapping inspection of SPAD value of rice canopy at booting stage (**a**) Booting stage-RVI(S_{Dr},S_{Db}); (**b**) Booting stage-PLSR; (**c**) Booting stage-SVR; (**d**) Booting stage-BP.

Comparing the statistical characteristics of the SPAD values on the prediction maps of each model (Table 13), it can be seen that the estimation of the SPAD value of the rice canopy by the univariate regression model as a whole is low and the mapping inspection at the milk-ripe stage is better than the booting stage. The PLSR model has an overly concentrated distribution of estimates of SPAD values. The SVR model has a discrete distribution of estimates of SPAD values, with over-estimation of high values and under-estimation of low values. The BP model works well overall, but there is an overfitting of individual cells.

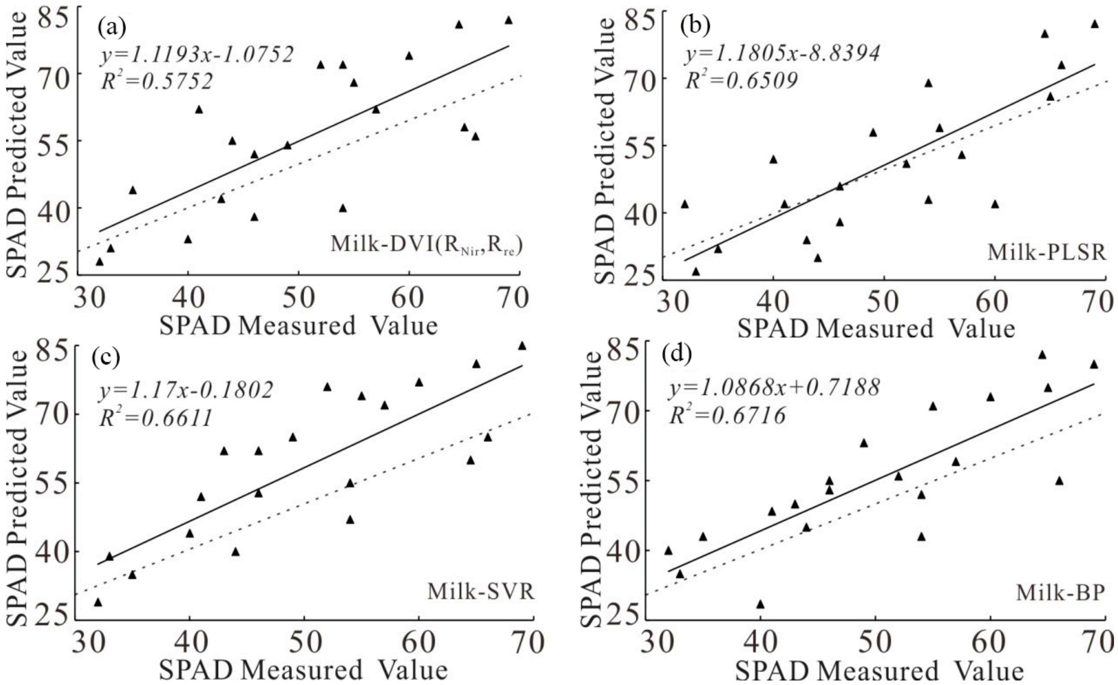

Figure 13. Mapping inspection of SPAD value of rice canopy at milk-ripe stage (**a**) Milk-ripe stage–DVI(R_{Nir},R_{re}); (**b**) Milk-ripe stage-PLSR; (**c**) Milk-ripe stage-SVR; (**d**) Milk-ripe stage-BP.

Based on the fitting results of the two growth periods (Table 14), the univariate regression model has the largest difference between the estimated value of SPAD and the measured value, and the inversion accuracy is low. This is due to the prevalence of both homogeneous and heterogeneous spectra on hyperspectral images. The univariate-based model cannot fully reflect the differences in SPAD values of different canopies due to the limited use of spectral information. Therefore, there are large errors in the SPAD values of rice canopies estimated by the model when generating inversion estimates. Since the PLSR, SVR and BP models use multiple spectral parameters as independent variables, the spectral information is used to a greater extent, which greatly reduces the errors caused by the same-spectrum foreign objects and the same-spectrum heterogeneous phenomena, so the prediction results are closer to the true value.

Table 14. Different model inversion accuracy tests for different fertility stages.

Growth Stages	Models	Gradient	R^2	RMSE	RE
Booting stage	RVI (S_{Dr},S_{Db})	1.2596	0.5511	9.1527	21.1
	PLSR	1.2584	0.6187	7.9526	18.6
	SVR	1.2551	0.6258	7.8599	20.6
	BP	1.2626	0.6206	7.9001	20.6
Milk-ripe stage	DVI (R_{Nir},R_{re})	1.1193	0.5752	11.1030	20.1
	PLSR	1.1805	0.6509	9.9778	19.6
	SVR	1.17	0.6611	9.6688	16.5
	BP	1.0868	0.6716	8.7710	15.8

By further comparing the three multiple regression models, PLSR also considers the independent variables, the principal components of the dependent variables and the degree of explanation of the independent variables by the dependent variables. Through principal component analysis, we can make the best use of spectral information so as to better achieve modeling accuracy and estimation effect. SVR adopts the idea of constructing the optimal hyperplane and uses the kernel function to avoid the nonlinear mapping displayed so as to solve the calculation difficulties caused by the high-dimensional space. The model is easy to train, and there is no local minimum value. Therefore, when the measured value of the SPAD value at the booting stage is small, a good inversion effect can be obtained. The BP neural network has the characteristics of self-learning, automatic adjustment and fault tolerance, and it has great advantages in dealing with nonlinear problems. By simulating the neural transmission feedback modulation, the training was repeated many times, and the final SPAD value prediction was closer to the measured value.

Based on the above charts and conclusions, this paper compares the effects of four different models to invert the SPAD value of a rice canopy and finally selects the optimal inversion model for the SPAD value of a rice canopy at different growth stages: "booting stage-SVR" and "milk-ripe stage-BP". This can prove that the use of an imaging hyperspectrometer mounted on the UAV platform can effectively identify the spectral information of rice, can achieve non-destructive, real-time and efficient monitoring of rice canopy SPAD values, and can be effectively applied to real life, providing scientific evidence for the development of precision agriculture.

4. Conclusions

In this study, we used an unmanned aerial vehicle (UAV)-based hyperspectral imager and a high-resolution camera to obtain hyperspectral images of a rice canopy at the low-altitude canopy scale; we analyzed the corresponding spectral features, extracted ten sensitive bands at the booting stage and eight sensitive bands at the milk-ripe stage, and established four estimation models. The model was applied to invert the hyperspectral images to obtain a visualization and quantitative distribution map of the SPAD values at the rice canopy scale. The inversion results are of high accuracy, which enables a comprehensive study from basic spectral analysis to the practical application of the model, thus providing an intuitive and quantitative interpretation basis for the monitoring of rice canopy SPAD values and diagnosis of health conditions. This proves that UAV-based remote sensing platforms can provide a scientific basis for decision-making for actual agricultural production. Similar conclusions were reached by Mingyang Ma [52], who concluded that inversion of SPAD using UAV HD imagery was feasible and that BP neural networks with multiple feature inputs based on NRI, B/R and R-B predicted SPAD in japonica rice with an 11% improvement in accuracy compared to the NRI-based one-dimensional linear regression analysis model. Songtao Ban [53] compared the chlorophyll content of rice in two different regions (Ningxia and Shanghai) using UAV-based spectral imagery and showed that the chlorophyll content of rice in both regions was significantly correlated with the reflectance of green, red and near-red-edge bands and eight vegetation indices including the normalized difference vegetation index (NDVI), and the PLSR model was more stable than SVR and ANN in estimating chlorophyll content. Yuan Weinan [54] proposed a different method for estimating chlorophyll in rice canopy leaves from this paper: he used UAV HD images, a dimensionality reduction method based on principal substrate analysis to construct a principal substrate with concentrated waveform information, and a least squares regression model for chlorophyll content estimation. The method is also important for the estimation of chlorophyll content of plant leaves.

In this study, although some results have been achieved in rice canopy SPAD value estimation using UAV hyperspectral images, the changes that cause the spectral characteristics of the rice canopy are multifactorial. Other biophysical and chemical parameters such as canopy water content, nitrogen content and leaf area index also affect their spectral variation. If the influence of many factors on spectral changes can be expressed in different weights, it will further improve the inversion accuracy of rice canopy SPAD values based on UAV hyperspectral data and enable better monitoring of rice growth status and dynamic changes in a comprehensive manner.

Author Contributions: Conceptualization, Methodology, H.L. (Hanhu Liu) and X.L.; Software, Validation and Formal analysis, X.W.; Investigation, Resources, Data curation and Writing—original preparation, H.L. (Hui Liang); Writing—review, Editing and Visualization, X.L. All authors have read and agreed to the published version of the manuscript.

Funding: This research received no external funding.

Institutional Review Board Statement: Not applicable.

Informed Consent Statement: Not applicable.

Data Availability Statement: Not applicable.

Acknowledgments: The authors are grateful for helpful comments from many researchers and colleagues.

Conflicts of Interest: The authors declare that they have no known competing financial interest or personal relationships that could have appeared to influence the work reported in this paper.

References

1. Hu, T.; Chen, Y.; Li, D.; Long, C.; Wen, Z.; Hu, R.; Chen, G. Rice Variety Identification Based on the Leaf Hyperspectral Feature via LPP-SVM. *Int. J. Pattern Recognit. Artif. Intell.* **2022**, *36*, 17. [CrossRef]
2. Luo, Y.; Huang, D.; Li, D.; Wu, L. On farm storage, storage losses and the effects of loss reduction in China. *Resour. Conserv. Recycl.* **2020**, *162*, 9. [CrossRef]
3. Xiao, X.M.; Boles, S.; Liu, J.Y. Mapping paddy rice agriculture in southern China using multi-temporal MODIS images. *Remote Sens. Environ.* **2005**, *95*, 480–492. [CrossRef]
4. Xu, Y.B.; Li, J.Y.; Wan, J.M. Agriculture and crop science in China: Innovation and sustainability. *Crop J.* **2017**, *5*, 95–99. [CrossRef]
5. Chen, T.; Fu, W.; Yu, J.; Feng, B.; Li, G.; Fu, G.; Tao, L. The Photosynthesis Characteristics of Colored Rice Leaves and Its Relation with Antioxidant Capacity andAnthocyanin Content. *Sci. Agric. Sin.* **2022**, *55*, 12.
6. Li, X.; Lu, X.; Xi, J.; Zhang, Y.; Zhang, M. Univeisal method to detect the chlorophyll content in plant leaves with RGB images captured by smart phones. *Trans. Chin. Soc. Agric. Eng.* **2021**, *37*, 7.
7. Ravier, C.; Quemada, M.; Jeuffroy, M.-H. Use of a chlorophyll meter to assess nitrogen nutrition index during the growth cycle in winter wheat. *Field Crops Res.* **2017**, *214*, 73–82. [CrossRef]
8. Ganeva, D.; Roumenina, E.; Dimitrov, P. Phenotypic Traits Estimation and Preliminary Yield Assessment in Different Phenophases of Wheat Breeding Experiment Based on UAV Multispectral Images. *Remote Sens.* **2022**, *14*, 1019. [CrossRef]
9. Filion, R.; Bernier, M.; Paniconi, C. Remote sensing for mapping soil moisture and drainage potential in semi-arid regions: Applications to the Campidano plain of Sardinia, Italy. *Sci. Total Environ.* **2016**, *543*, 862–876. [CrossRef]
10. Mulla, D.J. Twenty five years of remote sensing in precision agriculture: Key advances and remaining knowledge gaps. *Biosyst. Eng.* **2013**, *114*, 358–371. [CrossRef]
11. Weiss, M.; Jacob, F.; Duveiller, G. Remote sensing for agricultural applications: A meta-review. *Remote Sens. Environ.* **2020**, *236*, 111402. [CrossRef]
12. Tao, H.; Feng, H.; Xu, L.; Miao, M.; Long, H.; Yue, J.; Li, Z.; Yang, G.; Yang, X.; Fan, L. Estimation of Crop Growth Parameters Using UAV-Based Hyperspectral Remote Sensing Data. *Sensors* **2020**, *20*, 1296. [CrossRef] [PubMed]
13. Burkart, A.; Cogliati, S.; Schickling, A.; Rascher, U. A Novel UAV-Based Ultra-Light Weight Spectrometer for Field Spectroscopy. *IEEE Sens. J.* **2014**, *14*, 62–67. [CrossRef]
14. Wei, Z.; Han, Y.; Li, M.; Yang, K.; Yang, Y.; Luo, Y.; Ong, S.-H. A Small UAV Based Multi-Temporal Image Registration for Dynamic Agricultural Terrace Monitoring. *Remote Sens.* **2017**, *9*, 904. [CrossRef]
15. Huang, Y.; Ma, Q.; Wu, X.; Li, H.; Xu, K.; Ji, G.; Qian, F.; Li, L.; Huang, Q.; Long, Y.; et al. Estimation of chlorophyll content in Brassica napus based on unmanned aerial vehicle images. *Oil Crop Sci.* **2022**, *7*, 149–155. [CrossRef]
16. Kim, E.-J.; Nam, S.-H.; Koo, J.-W.; Hwang, T.-M. Hybrid Approach of Unmanned Aerial Vehicle and Unmanned Surface Vehicle for Assessment of Chlorophyll-a Imagery Using Spectral Indices in Stream, South Korea. *Water* **2021**, *13*, 1930. [CrossRef]
17. Ballesteros, R.; Ortega, J.F.; Hernández, D.; Moreno, M.A. Applications of georeferenced high-resolution images obtained with unmanned aerial vehicles. Part II: Application to maize and onion crops of a semi-arid region in Spain. *Precis. Agric.* **2014**, *15*, 593–614. [CrossRef]
18. Calderón, R.; Navas-Cortés, J.A.; Lucena, C.; Zarco-Tejada, P.J. High-resolution airborne hyperspectral and thermal imagery for early, detection of Verticillium wilt of olive using fluorescence, temperature and narrow-band spectral indices. *Remote Sens. Environ.* **2013**, *139*, 231–245. [CrossRef]
19. Panigrahi, N.; Das, B.S. Canopy Spectral Reflectance as a Predictor of Soil Water Potential in Rice. *Water Resour. Res.* **2018**, *54*, 2544–2560. [CrossRef]
20. Poblete-Echeverría, C.; Olmedo, G.F.; Ingram, B.; Bardeen, M. Detection and Segmentation of Vine Canopy in Ultra-High Spatial Resolution RGB Imagery Obtained from Unmanned Aerial Vehicle (UAV): A Case Study in a Commercial Vineyard. *Remote Sens.* **2017**, *9*, 268. [CrossRef]

21. Gitelson, A.A.; Peng, Y.; Arkebauer, T.J. Relationships between gross primary production, green LAI, and canopy chlorophyll content in maize: Implications for remote sensing of primary production. *Remote Sens. Environ.* **2014**, *144*, 65–72. [CrossRef]
22. He, Z.; Wu, K.; Wang, F.; Jin, L.; Zhang, R.; Tian, S.; Wu, W.; He, Y.; Huang, R.; Yuan, L.; et al. Fresh Yield Estimation of Spring Tea via Spectral Differences in UAV Hyperspectral Images from Unpicked and Picked Canopies. *Remote. Sens.* **2023**, *15*, 1100. [CrossRef]
23. Padalia, H.; Sinha, S.K.; Bhave, V.; Trivedi, N.K.; Kumar, A.S. Estimating canopy LAI and chlorophyll of tropical forest plantation (North India) using Sentinel-2 data. *Adv. Space Res.* **2020**, *65*, 458–469. [CrossRef]
24. Thomas, V.; Treitz, P.; McCaughey, J.H.; Noland, T.; Rich, L. Canopy chlorophyll concentration estimation using hyperspectral and lidar data for a boreal mixedwood forest in northern Ontario, Canada. *Int. J. Remote Sens.* **2008**, *29*, 1029–1052. [CrossRef]
25. Feng, M.C.; Guo, X.L.; Wang, C. Monitoring and evaluation in freeze stress of winter wheat (*Triticum aestivum* L.) through canopy hyperspectrum reflectance and multiple statistical analysis. *Ecol. Indic.* **2018**, *84*, 290–297. [CrossRef]
26. Shi, H.; Guo, J.; An, J.; Tang, Z.; Wang, X.; Li, W.; Zhao, X.; Jin, L.; Xiang, Y.; Li, Z.; et al. Estimation of Chlorophyll Content in Soybean Crop at Different Growth Stages Based on Optimal Spectral Index. *Agronomy* **2023**, *13*, 663. [CrossRef]
27. Liang, L.; Qin, Z.; Zhao, S.; Di, L.; Zhang, C.; Deng, M.; Lin, H.; Zhang, L.; Wang, L.; Liu, Z. Estimating crop chlorophyll content with hyperspectral vegetation indices and the hybrid inversion method. *Int. J. Remote Sens.* **2016**, *37*, 2923–2949. [CrossRef]
28. Milas, A.S.; Romanko, M.; Reil, P.; Abeysinghe, T.; Marambe, A. The importance of leaf area index in mapping chlorophyll content of corn under different agricultural treatments using UAV images. *Int. J. Remote Sens.* **2018**, *39*, 5415–5431. [CrossRef]
29. Wu, C.; Han, X.; Niu, Z.; Dong, J. An evaluation of EO-1 hyperspectral Hyperion data for chlorophyll content and leaf area index estimation. *Int. J. Remote Sens.* **2010**, *31*, 1079–1086. [CrossRef]
30. Fageria, N.K. Yield physiology of rice. *J. Plant Nutr.* **2007**, *30*, 843–879. [CrossRef]
31. Hlaváčová, M.; Klem, K.; Rapantová, B.; Novotná, K.; Urban, O.; Hlavinka, P.; Smutná, P.; Horáková, V.; Škarpa, P.; Pohanková, E.; et al. Interactive effects of high temperature and drought stress during stem elongation, anthesis and early grain filling on the yield formation and photosynthesis of winter wheat. *Field Crops Res.* **2018**, *221*, 182–195. [CrossRef]
32. Guo, C.; Guo, X. Estimation of wetland plant leaf chlorophyll content based on continuum removal in the visible domain. *Acta Ecol. Sin.* **2016**, *36*, 6538–6546.
33. Guo, Q.; Wu, X.; Bing, Q.; Pan, Y.; Wang, Z.; Fu, Y.; Wang, D.; Liu, J. Study on Retrieval of Chlorophyll-a Concentration Based on Landsat OLI Imagery in the Haihe River, China. *Sustainability* **2016**, *8*, 758. [CrossRef]
34. Matus-Hernández, M.; Hernández-Saavedra, N.Y.; Martínez-Rincón, R.O. Predictive performance of regression models to estimate Chlorophyll-a concentration based on Landsat imagery. *PLoS ONE* **2018**, *13*, e0205682. [CrossRef]
35. Ryan, K.; Ali, K. Application of a partial least-squares regression model to retrieve chlorophyll-aconcentrations in coastal waters using hyper-spectral data. *Ocean Ence J.* **2016**, *51*, 209–221.
36. Song, K.; Lu, D.; Li, L.; Li, S.; Wang, Z.; Du, J. Remote sensing of chlorophyll-a concentration for drinking water source using genetic algorithms (GA)-partial least square (PLS) modeling. *Ecol. Inform.* **2012**, *10*, 25–36. [CrossRef]
37. Kown, Y.; Baek, S.H.; Lim, Y.K.; Pyo, J.; Ligaray, M.; Park, Y.; Cho, K.H. Monitoring Coastal Chlorophyll-a Concentrations in Coastal Areas Using Machine Learning Models. *Water* **2018**, *10*, 1020. [CrossRef]
38. Shao, Y.-H.; Chen, W.-J.; Deng, N.-Y. Nonparallel hyperplane support vector machine for binary classification problems. *Inf. Sci.* **2014**, *263*, 22–35. [CrossRef]
39. Liu, M.; Liu, X.; Li, M.; Fang, M.; Chi, W. Neural-network model for estimating leaf chlorophyll concentration in rice under stress from heavy metals using four spectral indices. *Biosyst. Eng.* **2010**, *106*, 223–233. [CrossRef]
40. Lu, F.; Chen, Z.; Liu, W.; Shao, H. Modeling chlorophyll-a concentrations using an artificial neural network for precisely eco-restoring lake basin. *Ecol. Eng.* **2016**, *95*, 422–429. [CrossRef]
41. Buma, B. Evaluating the utility and seasonality of NDVI values for assessing post-disturbance recovery in a subalpine forest. *Environ. Monit. Assess.* **2012**, *184*, 3849–3860. [CrossRef] [PubMed]
42. Gitelson, A.A.; Kaufman, Y.J.; Merzlyak, M.N. Use of a green channel in remote sensing of global vegetation from EOS-MODIS. *Remote Sens. Environ.* **1996**, *58*, 289–298. [CrossRef]
43. Aasen, H.; Burkart, A.; Bolten, A. Generating 3D hyperspectral information with lightweight UAV snapshot cameras for vegetation monitoring: From camera calibration to quality assurance. *ISPRS J. Photogramm. Remote Sens.* **2015**, *108*, 245–259. [CrossRef]
44. Haboudane, D.; Miller, J.R.; Tremblay, N.; Zarco-Tejada, P.J.; Dextraze, L. Integrated narrow-band vegetation indices for prediction of crop chlorophyll content for application to precision agriculture. *Remote Sens. Environ.* **2002**, *81*, 416–426. [CrossRef]
45. Daughtry, C.S.T.; Walthall, C.L.; Kim, M.S. Estimating corn leaf chlorophyll concentration from leaf and canopy reflectance. *Remote Sens. Environ.* **2000**, *74*, 229–239. [CrossRef]
46. Rodger, A.; Laukamp, C.; Haest, M.; Cudahy, T. A simple quadratic method of absorption feature wavelength estimation in continuum removed spectra. *Remote Sens. Environ.* **2012**, *118*, 273–283. [CrossRef]
47. Dash, J.; Curran, P.J. Evaluation of the MERIS terrestrial chlorophyll index (MTCI). *Adv. Space Res.* **2007**, *39*, 100–104. [CrossRef]
48. Cao, Q.; Miao, Y.X.; Shen, J.N. Improving in-season estimation of rice yield potential and responsiveness to topdressing nitrogen application with Crop Circle active crop canopy sensor. *Precis. Agric.* **2016**, *17*, 136–154. [CrossRef]
49. Wang, F.-m.; Huang, J.-f.; Tang, Y.-l.; Wang, X.-z. New Vegetation Index and Its Application in Estimating Leaf Area Index of Rice. *Rice Sci.* **2007**, *14*, 195–203. [CrossRef]

50. Gitelson, A.A.; Viña, A.; Ciganda, V.; Rundquist, D.C.; Arkebauer, T.J. Remote estimation of canopy chlorophyll content in crops. *Geophys. Res. Lett.* **2005**, *32*, L08403. [CrossRef]
51. Kanke, Y.; Tubaña, B.; Dalen, M.; Harrell, D. Evaluation of red and red-edge reflectance-based vegetation indices for rice biomass and grain yield prediction models in paddy fields. *Precis. Agric.* **2016**, *17*, 507–530. [CrossRef]
52. Ma, M.; Xu, T.; Zhou, Y. UAV HD Image Detection Method for SPAD in Northeast Japonica Rice. *J. Shenyang Agric. Univ.* **2017**, *48*, 757–762.
53. Ban, S.; Liu, W.; Tian, M.; Wang, Q.; Yuan, T.; Chang, Q.; Li, L. Rice Leaf Chlorophyll Content Estimation Using UAV-Based Spectral Images in Different Regions. *Agronomy* **2022**, *12*, 2832. [CrossRef]
54. Yuan, W.; Xu, T.; Cao, Y. Estimation of chlorophyll content in rice canopy leaves based on main base analysis and dimensionality reduction method. *J. Zhejiang Univ. Agric. Life Sci.* **2018**, *44*, 423–430.